中国光学（中英文） Chinese Optics 核心期刊

Design method for conformal systems based on plane-symmetric aberration theory

YAN Shu-run, WANG Jiang-nan, GUO Xiao-tong, KANG Ze-feng, MENG Qing-yu

Citation:
YAN Shu-run, WANG Jiang-nan, GUO Xiao-tong, KANG Ze-feng, MENG Qing-yu. Design method for conformal systems based on plane-symmetric aberration theory[J]. *Chinese Optics*, In press. doi: 10.37188/CO.EN-2025-0044
严舒润, 王江南, 郭晓彤, 康泽锋, 孟庆宇. 基于平面对称系统像差理论的共形光学系统设计方法[J]. 中国光学, 优先发表. doi: 10.37188/CO.EN-2025-0044

View online: https://doi.org/10.37188/CO.EN-2025-0044

文章编号　2097-1842(xxxx)x-0001-18

Design method for conformal systems based on plane-symmetric aberration theory

YAN Shu-run[1,2], WANG Jiang-nan[1,2], GUO Xiao-tong[1,2], KANG Ze-feng[1,2], MENG Qing-yu[1 *]

（1. *Changchun Institute of Optics*, *Fine Mechanics and Physics*, *Chinese Academy of Sciences*, *Changchun* 130033, *China*;

2. *University of Chinese Academy of Science*, *Beijing* 100049, *China*）

* *Corresponding author*, *E-mail*: *mengqy@ciomp.ac.cn*

Abstract: The design of conformal optical systems often suffers from insufficient theoretical guidance, resulting in repeated trial-and-error optimization. To address this, we introduce a design method based on aberration theory for plane-symmetric systems. By converting global surface parameters into local surface parameters, the aberration theory is generalized to conformal systems, enabling analytical calculation of each surface's aberration contribution. Using this formulation, we propose a two-step design strategy. First, the optimal gimbal position is determined by minimizing the aberration contribution of the dome's outer surface. Second, during arch-corrector optimization, freeform parameters associated with dominant aberrations are progressively introduced, and an aberration-coefficient-based merit function is employed. To validate the effectiveness of the proposed method, comparative designs of 14 conformal systems were completed for identical specifications across different gimbal positions and optimization approaches. Results demonstrate that the system designed using our method achieves a full-field modulation transfer function (MTF) exceeding 0.4 at a spatial frequency of 42 lp/mm, with imaging quality approaching the diffraction limit—representing a 2.4× improvement over conventional design methods. This approach provides systematic theoretical guidance for the design of high-performance conformal optical systems.

Key words: conformal optics; aberration theory; freeform optics

收稿日期:2025-12-02; **修订日期**:xxxx-xx-xx

基金项目:中国科学院战略性先导科技专项(No. XDB1050200); 国家自然科学基金(No. 62375264); 中国科学院青年创新促进会(No. Y2023061)资助

Supported by Strategic Priority Research Program of the Chinese Academy of Sciences (No. XDB1050200); National Natural Science Foundation of China (No. 62375264); Youth Innovation Promotion Association of the Chinese Academy of Sciences (No. Y2023061)

基于平面对称系统像差理论的共形光学系统设计方法

严舒润[1,2], 王江南[1,2], 郭晓彤[1,2], 康泽锋[1,2], 孟庆宇[1*]
（1. 中国科学院长春光学精密机械与物理研究所, 吉林 长春 130033；
2. 中国科学院大学, 北京 100049）

摘要: 针对共形光学系统设计中理论指导不足、过度依赖试错优化的问题, 本文提出一种基于平面对称系统像差理论的设计方法。通过建立全局面型参数与局域面型参数的转换关系, 将现有像差理论拓展至共形系统, 实现了各表面像差贡献的解析计算。基于该理论框架, 构建了两步式设计策略: 首先, 通过分析整流罩外表面的像差贡献分布规律, 选取像差贡献最小的万向节点位置作为系统初始结构; 其次, 在拱形校正器优化过程中, 逐步引入与像差相关的自由曲面参数, 并构建像差系数评价函数。为验证方法的有效性, 对同一设计指标组合不同万向节点位置与优化方法, 完成 14 组共形系统的对比设计。结果表明: 采用本文方法设计的系统在 42 lp/mm 空间频率处全视场调制传递函数(MTF)优于 0.4, 成像质量接近衍射极限, 性能达到传统设计方法的 2.4 倍。该方法为高性能共形光学系统设计提供了系统的理论指导。

关　键　词: 共形光学; 像差理论; 自由曲面
中图分类号: O482.31　　**文献标志码:** A　　**doi:** 10.37188/CO.EN-2025-0044　　**CSTR:** 32171.14.CO.EN-2025-0044

1 Introduction

Modern missile domes have evolved from traditional hemispherical shapes to streamlined profiles to achieve superior aerodynamic performance. A conformal optical system is defined as one where non-imaging performance metrics, such as aerodynamic characteristics, take design priority. In missile seekers operating in scanning mode, the imaging system inside the dome rotates about a gimbal point. For any given look angle, only a localized region of the dome participates in imaging, and this region shifts with the changing perspective, giving rise to aberrations that exhibit look-angle dependence—referred to as dynamic aberrations. The correction of these dynamic aberrations represents the central challenge in conformal optical system design.

When the look angle is non-zero, the dome's imaging region loses its rotational symmetry, rendering conventional Seidel aberration theory inadequate. Researchers have widely adopted Zernike polynomials to characterize the aberration properties of conformal systems, with investigations covering various dome profiles, including conicoidal surfaces[1-3], von Karman surfaces[4-5], and Haack surfaces[6]. With the advancement of aberration theory, several computational methods for non-rotationally symmetric systems have emerged in recent years, such as nodal aberration theory[7-10], the Lie algebraic method[11], and analytical methods[12-14]. These approaches have been successfully applied to the design of off-axis three-mirror systems[15-16], spectrometers[13], and soft X-ray/vacuum ultraviolet optical systems[17]. However, to the best of our knowledge based on currently published literature, no studies have yet reported the application of non-rotationally symmetric system aberration theory to conformal optical systems.

To correct the dynamic aberrations introduced by conformal domes, corrective elements must be inserted between the dome and the imaging system. Classical aberration correctors can be categorized into three types: fixed, moving, and arch correctors. Among these, the arch corrector offers distinct advantages by combining the flexibility of an asymmetric profile with the reliability of a motor-free

mechanism. Its initial configuration can be obtained through numerical solution of the Wassermann–Wolf differential equation, followed by optimization to achieve the final design[18]. In recent years, alternative aberration correction schemes have also been proposed, including lens arrays[19-20], diffractive surfaces[21], dome profile optimization[22-23], and wavefront coding[24-25]. Nevertheless, these alternatives still face limitations in manufacturing complexity, cost, or response speed, whereas the fabrication and metrology technologies for arch correctors have become relatively mature[26], making them the current mainstream solution.

Despite significant progress in conformal optics research, existing design methodologies still suffer from insufficient theoretical guidance and excessive reliance on trial-and-error optimization and empirical judgment. Current Zernike-based aberration analysis remains limited to characterizing the total system aberration, preventing designers from analytically calculating the aberration contribution of a single surface based on its profile parameters. This theoretical deficiency makes it extremely difficult to efficiently adjust surface parameters to target specific aberration types, resulting in a highly experience-dependent design process.

To overcome these limitations, this paper expands the plane-symmetric system aberration theory and proposes a conformal optical system design methodology based on analytical aberration computation, thereby providing theoretical support throughout the design process. Section 2 derives the conversion relationship between global and local surface parameters, extending the plane-symmetric aberration theory to conformal systems. Section 3 elaborates on the first step of the proposed method: determining the optimal gimbal point position by minimizing the aberration contribution from the dome's outer surface, thereby establishing a theoretical criterion for initial configuration selection. Section 4 addresses the second step: progressively introducing aberration-related freeform surface parameters as optimization variables and constructing an aberration-coefficient-based merit function for efficient arch corrector optimization. Section 5 validates the significant imaging quality improvements through comparative analysis with conventional design approaches.

2 Extension of plane-symmetric aberration theory

2.1 Existing aberration theory

Sasián[27] established an aberration expression for plane-symmetric systems, given as

$$W(\boldsymbol{H},\boldsymbol{\rho}) = \sum_{k,m,n,p,q}^{\infty} W_{i,j,n,p,q} (\boldsymbol{H}\cdot\boldsymbol{H})^k (\boldsymbol{\rho}\cdot\boldsymbol{\rho})^m (\boldsymbol{H}\cdot\boldsymbol{\rho})^n (\boldsymbol{i}\cdot\boldsymbol{H})^p (\boldsymbol{i}\cdot\boldsymbol{\rho})^q \quad , \tag{1}$$

where the subindices satisfy $i = 2k+n+p$ and $j = 2m+n+q$, and $W_{i,j,n,p,q}$ are the corresponding aberration coefficients. The vector $\boldsymbol{i}$ is the symmetry unit vector directed along the positive Y axis. Compared to rotationally symmetric systems, plane-symmetric systems include additional terms $(\boldsymbol{i}\cdot\boldsymbol{H})^p$ and $(\boldsymbol{i}\cdot\boldsymbol{\rho})^q$, leading to more aberration types.

Aberration terms are grouped by the number of dot products, $k+m+n+p+q$. In Tab. 1, the first three groups of aberrations are shown. The terminology constant, linear, quadratic, etc. refer to the field dependence of the aberration term. When $p,q=0$, $W_{i,j,n,0,0}$ reduces to the aberration coefficients of rotationally symmetric systems (i.e., the bottom rows of Tab. 1).

Liu[13] analytically evaluated the surface contributions of aberration coefficients by combining local surface parameters with raytracing data. The local surface profile is a freeform surface symmetric about the YZ-plane with a spherical base, and its fourth-order approximation can be expressed as

$$z' \approx \frac{r'^2}{2R_x} + \frac{r'^4}{8R_x^3} + F_{02}y'^2 + F_{21}x'^2y' + F_{03}y'^3 + F_{40}x'^4 + F_{22}x'^2y'^2 + F_{04}y'^4 \quad , \tag{2}$$

where $r'^2 = x'^2 + y'^2$, with x', y' being the coordin-

ates in the local coordinate system, and z' representing the sag. R_x is the sagittal radius of curvature, and F_{02}, F_{21}, F_{03}, F_{40}, F_{22}, F_{04} are freeform coefficients, collectively referred to as local surface parameters. Since high-order surface parameters have no contribution to the third group aberrations[13], it is sufficient to expand the local surface to the fourth order.

Tab. 1 Aberration terms in plane-symmetric systems

Group	Vector form	Name
First group	W_{00000}	Constant piston
Second group	$W_{01001}(\boldsymbol{i}\cdot\boldsymbol{\rho})$	Field displacement
	$W_{10010}(\boldsymbol{i}\cdot\boldsymbol{H})$	Linear piston
	$W_{02000}(\boldsymbol{\rho}\cdot\boldsymbol{\rho})$	Defocus
	$W_{11100}(\boldsymbol{H}\cdot\boldsymbol{\rho})$	Magnification
	$W_{20000}(\boldsymbol{H}\cdot\boldsymbol{H})$	Quadratic piston
Third group	$W_{02002}(\boldsymbol{i}\cdot\boldsymbol{\rho})^2$	Constant astigmatism
	$W_{11011}(\boldsymbol{i}\cdot\boldsymbol{H})(\boldsymbol{i}\cdot\boldsymbol{\rho})$	Anamorphism
	$W_{20020}(\boldsymbol{i}\cdot\boldsymbol{H})^2$	Quadratic piston
	$W_{03001}(\boldsymbol{i}\cdot\boldsymbol{\rho})(\boldsymbol{\rho}\cdot\boldsymbol{\rho})$	Constant coma
	$W_{12101}(\boldsymbol{i}\cdot\boldsymbol{\rho})(\boldsymbol{H}\cdot\boldsymbol{\rho})$	Linear astigmatism
	$W_{12010}(\boldsymbol{i}\cdot\boldsymbol{H})(\boldsymbol{\rho}\cdot\boldsymbol{\rho})$	Field tilt
	$W_{21001}(\boldsymbol{i}\cdot\boldsymbol{\rho})(\boldsymbol{H}\cdot\boldsymbol{H})$	Quadratic distortion I
	$W_{21110}(\boldsymbol{i}\cdot\boldsymbol{H})(\boldsymbol{H}\cdot\boldsymbol{\rho})$	Quadratic distortion II
	$W_{30010}(\boldsymbol{i}\cdot\boldsymbol{H})(\boldsymbol{H}\cdot\boldsymbol{H})$	Cubic piston
	$W_{04000}(\boldsymbol{\rho}\cdot\boldsymbol{\rho})^2$	Spherical aberration
	$W_{13100}(\boldsymbol{H}\cdot\boldsymbol{\rho})(\boldsymbol{\rho}\cdot\boldsymbol{\rho})$	Linear coma
	$W_{22200}(\boldsymbol{H}\cdot\boldsymbol{\rho})^2$	Quadratic astigmatism
	$W_{22000}(\boldsymbol{H}\cdot\boldsymbol{H})(\boldsymbol{\rho}\cdot\boldsymbol{\rho})$	Field curvature
	$W_{31100}(\boldsymbol{H}\cdot\boldsymbol{H})(\boldsymbol{H}\cdot\boldsymbol{\rho})$	Cubic distortion
	$W_{40000}(\boldsymbol{H}\cdot\boldsymbol{H})^2$	Quartic piston

The raytracing data consist of three rays. A real raytracing is performed for the optical axis ray (OAR) to obtain the incident and refracted angles I and I'. Paraxial raytracing is carried out for the sagittal marginal ray and the chief ray, yielding the ray heights x_a, x_b and the ray angles tangent u_{ax}, u'_{ax}, u_{bx}, u'_{bx}. The paraxial raytracing equations in the sagittal direction are given by

$$x_{i+1} = x_i + u'_{xi}t_i \quad , \tag{3}$$

$$n'_i u'_{xi} = n_i u_{xi} - x_i \phi_{xi} \quad , \tag{4}$$

$$u_{xi+1} = u'_{xi} \quad , \tag{5}$$

where ϕ_{xi} is the optical power of the surface in the sagittal direction, given as

$$\phi_{xi} = \frac{n'_i \cos I'_i - n_i \cos I_i}{R_{xi}} \quad , \tag{6}$$

Aberrations consist of intrinsic and induced components. The relationship between the local surface parameters and the aberration coefficients can be readily identified from the analytical expression of the intrinsic aberration. For example, the surface contributions to W_{02002} and W_{03001} are shown below:

$$W_{02002} = -\frac{1}{2}\Delta\left(\frac{u_{ax}C}{n}\right)\frac{x_a}{\cos^2 I'} + \Delta(n\cos I)F_{02}\frac{x_a^2}{\cos^2 I'} \quad , \tag{7}$$

$$\begin{aligned} W_{03001} = & \\ & -\frac{A}{2}\Delta\left(\frac{u_{ax}C}{n}\right)\frac{x_a}{\cos I'} - \frac{1}{2R_x}\Delta\left(\frac{u_{ax}C^2}{n}\right)\frac{x_a^2\tan I'}{\cos I'} + \\ & \Delta(n\cos I)\left(F_{21} + F_{02}\frac{\tan I'}{R_x}\right)\frac{x_a^3}{\cos I'} \quad , \end{aligned} \tag{8}$$

where the operator $\Delta(\cdot)$ denotes the change after refraction, and A, C are refraction invariants expressed as

$$A = n\left(u_{ax} + \frac{x_a\cos I}{R_x}\right) \quad , \tag{9}$$

$$C = n\sin I \quad , \tag{10}$$

It can be observed that W_{02002} is mainly related to the local surface parameters F_{02}, while W_{03001} mainly depends on F_{21}. This analytical relationship lays the theoretical foundation for aberration analysis and surface shape optimization of conformal systems.

2.2 Extension to conformal systems

In the existing aberration theory, surface profiles are described in a local coordinate system whose origin lies at the intersection of the surface and the OAR, with the local Z axis aligned with the surface normal at this point. However, optical

design software typically defines surfaces in a global coordinate system whose origin is at the vertex and Z axis aligns with the vertex normal. Fig. 1 illustrates these frames: XYZ denotes the global system and X'Y'Z' the local system. In a conformal system, for nonzero look angles (LA), the OAR does not pass through the vertex, meaning the global and local coordinate systems do not coincide. Therefore, to apply the aberration theory, global parameters must be transformed to local parameters.

Common global surfaces for conformal systems include conic, aspheric, and freeform surfaces. In this subsection, we derive the conversion formulas for conic surfaces; derivations for aspheric and XY-polynomial freeform surfaces are provided in Supplement.

The global surface expression for a conic is

$$z = \frac{cr^2}{1+\sqrt{1-(1+k)c^2r^2}} \quad , \qquad (11)$$

where $r^2 = x^2 + y^2$, with x, y being the coordinates in the global coordinate system, and z representing the sag. c is the curvature at the vertex, and k is the conic coefficient. The local surface expression is given by Eq. (2). The goal is to derive local surface parameters R_x, F_{02}, F_{21}, F_{03}, F_{40}, F_{22}, F_{04} from global surface parameters c, k and the OAR intersection point coordinates $(0, y_0, z_0)$.

The surface equation satisfied by the global surface profile is $F(x,y,z) = 0$. For a conic surface, this becomes:

$$F(x,y,z) = z^2(1+k)c - 2z + c\left(x^2+y^2\right) = 0 \quad , (12)$$

As shown in Fig. 1 (b), the global coordinate system is first translated to $(0, y_0, z_0)$, and then rotated by α degrees to obtain the local coordinate system. Therefore, the relationship between the global coordinates x,y,z and the local coordinates x',y',z' is

$$\begin{cases} x = x' \\ y = \cos\alpha y' + \sin\alpha z' + y_0 \\ z = -\sin\alpha y' + \cos\alpha z' + z_0 \end{cases} \quad , \qquad (13)$$

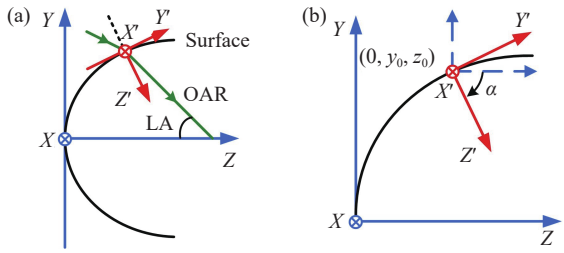

Fig. 1 Global coordinate system (XYZ) and local coordinate system (X'Y'Z'). (a) Overall view. (b) Enlarged view.

Substituting Eq. (13) into Eq. (12), we can obtain the surface equation satisfied by the local surface profile, given as

$$\begin{aligned} G(x',y',z') =& (-\sin\alpha y' + \cos\alpha z' + z_0)^2(1+k)c - \\ & 2(-\sin\alpha y' + \cos\alpha z' + z_0) + \\ & c\left[x'^2 + (\cos\alpha y' + \sin\alpha z' + y_0)^2\right] = \\ & 0 \quad , \end{aligned} \qquad (14)$$

where $z_0, \sin\alpha, \cos\alpha$ can be expressed as functions of y_0, given as

$$z_0 = \frac{1-\sqrt{1-(1+k)c^2y_0^2}}{(1+k)c} \quad , \qquad (15)$$

$$\sin\alpha = \frac{-cy_0}{\sqrt{1-kc^2y_0^2}} \quad , \qquad (16)$$

$$\cos\alpha = \frac{\sqrt{1-(1+k)c^2y_0^2}}{\sqrt{1-kc^2y_0^2}} \quad , \qquad (17)$$

Substituting Eqs. (15)–(17) into Eq. (14) and simplifying yields:

$$\begin{aligned} G(x',y',z') =& cx'^2 + \frac{cy'^2}{1-c^2ky_0^2} - 2z'\sqrt{1-c^2ky_0^2} + \\ & y'z'\frac{2c^2ky_0\sqrt{1-c^2(1+k)y_0^2}}{1-c^2ky_0^2} - \\ & z'^2\frac{c\left[-1+c^2k^2y_0^2+k\left(-1+2c^2y_0^2\right)\right]}{1-c^2ky_0^2} = \\ & 0 \quad , \end{aligned} \qquad (18)$$

Substituting the local surface expression Eq. (2) into the above equation results in a polynomial $G(x',y') = 0$, which contains the terms x'^2, y'^2, x'^2y', y'^3, x'^4, $x'^2y'^2$, y'^4. By setting each coeffi-

cient to zero, we can solve for the expressions of the local surface parameters:

$$R_x = \frac{\sqrt{1-c^2ky_0^2}}{c} \quad , \qquad (19)$$

$$F_{02} = \frac{c^3ky_0^2}{2\left(1-c^2ky_0^2\right)^{3/2}} \quad , \qquad (20)$$

$$F_{21} = \frac{c^3ky_0\sqrt{1-c^2(1+k)y_0^2}}{2\left(1-c^2ky_0^2\right)^{2}} \quad , \qquad (21)$$

$$F_{03} = \frac{c^3ky_0\sqrt{1-c^2(1+k)y_0^2}}{2\left(1-c^2ky_0^2\right)^{3}} \quad , \qquad (22)$$

$$F_{40} = \frac{c^3k-c^5k(1+k)y_0^2}{8\left(1-c^2ky_0^2\right)^{5/2}} \quad , \qquad (23)$$

$$F_{22} = \frac{c^3k\left[1+c^2ky_0^2-c^4k(3+2k)y_0^4\right]}{4\left(1-c^2ky_0^2\right)^{7/2}} \quad , \qquad (24)$$

$$F_{04} = c^3k\left[1+(1+3k)c^2y_0^2-k(7+4k)c^4y_0^4+k^2c^6y_0^6\right]/\left[8\left(1-c^2ky_0^2\right)^{9/2}\right] \quad , \qquad (25)$$

Thus, the local surface parameters R_x, F_{02}, F_{21}, F_{03}, F_{40}, F_{22}, F_{04} are completely expressed in terms of the global surface parameters c, k and the intersection coordinate y_0, completing the derivation of the surface parameter transformation. Combined with ray tracing data, the aberration contributions of each surface can now be calculated analytically.

3 Gimbal position selection

Fig. 2 illustrates a schematic representation of a conformal optical system. The imaging system is mounted on a gimbal, with the pivot angle referred to as the look angle (LA). The maximum LA defines the field of regard (FOR). Once the dome's geometric profile is determined, the gimbal position becomes the primary factor influencing the initial system configuration.

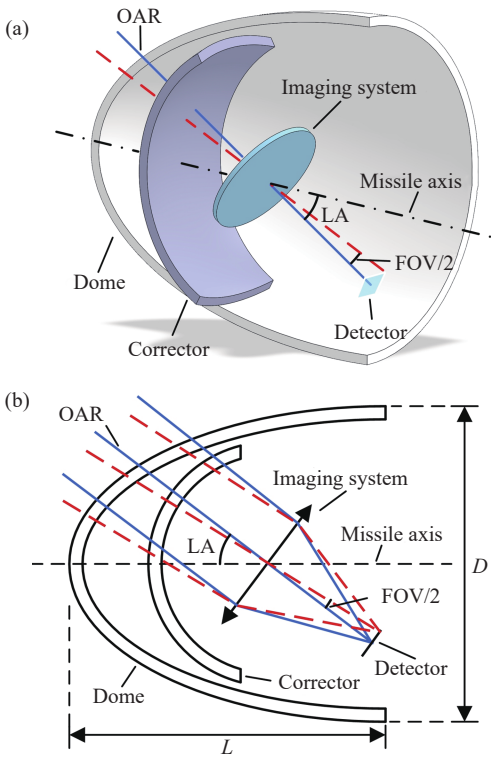

Fig. 2 Schematic diagram of a conformal system. (a) 3D layout. (b) 2D layout.

Previous studies have examined the influence of gimbal position on the total system aberration, concluding that its effect is relatively minor[3]. However, analyzing only the total system aberration is insufficient. The total aberration represents the residual after balancing contributions from the outer and inner surfaces of the dome, and is less correlated with the dome's geometric characteristics. To gain deeper insight, we investigate the relationship between gimbal position and the aberration contribution of the dome's outer surface, leading to new findings.

An ellipsoidal dome serves as an example for analysis, with length of 180 mm, fineness ratio of 1, global surface parameters of $R = 45$ mm, $k = -0.75$, and fabricated from ZnS. The imaging system is an approximate ideal two-mirror configuration, with the aperture stop located on the primary mirror. The gimbal point is positioned at the vertex of the secondary mirror. Fig. 3 shows system layouts for gimbal point distances of 60 mm and 120 mm from the dome vertex. For a constant FOR, a gimbal point closer to the dome vertex results in the imaging region being concentrated near the dome's apex.

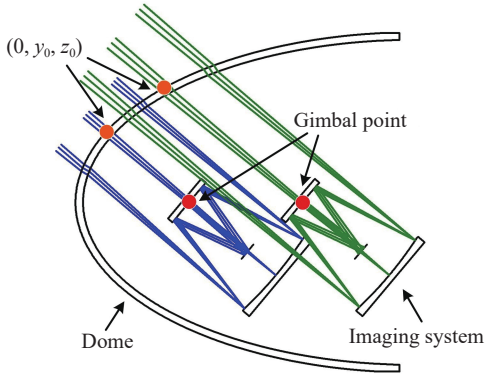

Fig. 3 Layouts of different gimbal positions.

Given that the dominant aberration types in conformal systems are constant astigmatism and constant coma[1-3], we focus on the corresponding aberration coefficients W_{02002} and W_{03001}. The local surface parameters exerting the most significant influence on these aberrations are F_{02} and F_{21}, respectively. According to Eqs. (20) and (21), these parameters depend on the local coordinate origin y_0, and their functional behavior is plotted in Fig. 4, where L_{GP} denotes the distance between the gimbal point and the dome vertex. Fig. 4 indicates that for FOR = ±40° and L_{GP} = 60 120 mm, increasing the gimbal point distance from the vertex enlarges the dynamic range of F_{02}, while the dynamic range of F_{21} remains relatively constant due to an extreme point.

This geometric characteristic leads to a significant increase in the dynamic range of W_{02002} with increasing L_{GP}, whereas the dynamic range of W_{03001} remains nearly unchanged, as shown in Fig. 5 and Fig. 6. Overall, a gimbal point closer to the dome vertex minimizes the surface aberration contribution from the dome.

Substantial aberration contributions from individual surfaces are often accompanied by higher-order induced aberrations, making the compensation of aberration challenging. Consequently, experienced designers advocate for "relaxed" optical systems, where each surface introduces minimal aberration[28]. Adhering to this design principle, we recommend selecting the gimbal position as close as practicable to the dome vertex when choosing the initial structure. For the exemplary ellipsoidal dome, L_{GP} = 60 mm is identified as the optimal gimbal position.

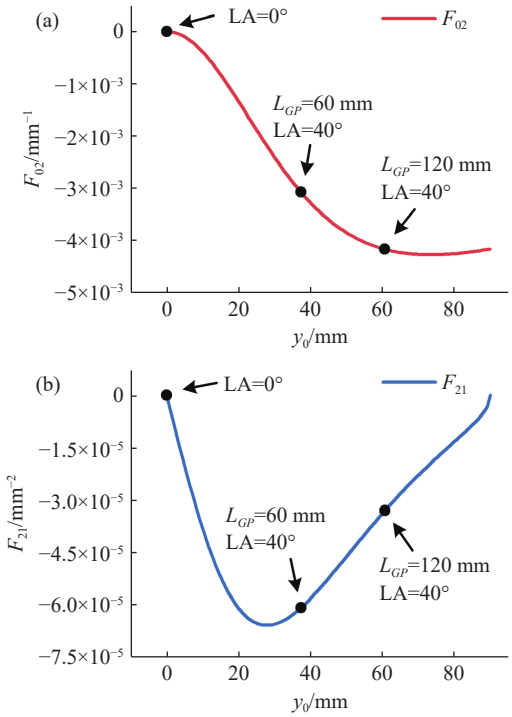

Fig. 4 Local surface parameters of the dome's outer surface. (a) Freeform parameter F_{02}. (b) Freeform parameter F_{21}.

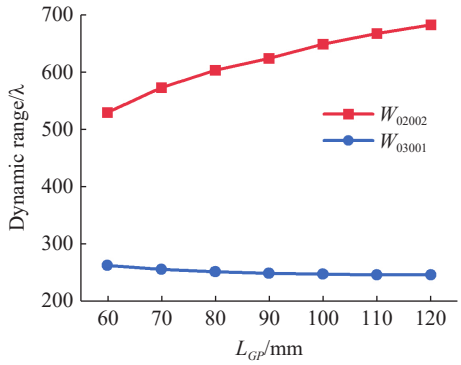

Fig. 5 Dynamic range of aberration surface contribution at different L_{GP}.

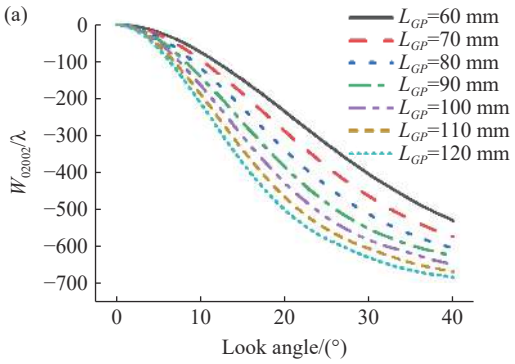

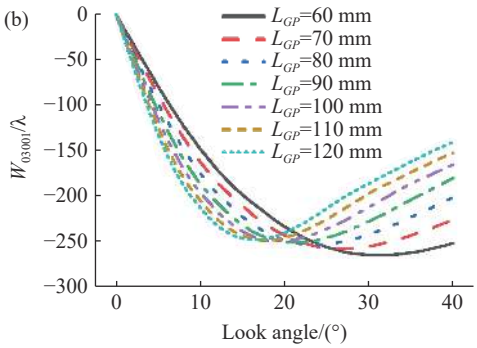

Fig. 6 Variation of aberration surface contribution with gimbal position. (a) W_{02002}. (b) W_{03001}.

4 Arch corrector optimization

4.1 Progressive introduction of optimization variables

The arch corrector comprises freeform surfaces possessing double-plane symmetry. Its global surface expression is given by:

$$z=\frac{cr^2}{1+\sqrt{1-(1+k)c^2r^2}}+\sum_{i,j=0}^{5}A_{2i,2j}x^{2i}y^{2j} \quad , \quad (26)$$

where $r^2=x^2+y^2$, with x, y being the coordinates in the global coordinate system, and z representing the sag. c is the curvature at the vertex, and k is the conic coefficient. $A_{2i,2j}$ are the freeform coefficients for the term $x^{2i}y^{2j}$. Due to the system's double symmetry about the YZ and XZ planes, the expression contains only even powers of x and y.

To apply the aberration theory, conversion from global to local surface parameters is necessary. The conversion formulas for F_{02} and F_{21} are as follows:

$$F_{02}=\left\{-2P_1^{(1)2}-k\left[1+2P_1^{(1)2}-4\left(P_1^{(2)}-P_2^{(2)}\right)\left(P^{(0)}-z_0\right)\right]+4\left(P_1^{(2)}-P_2^{(2)}\right)\left(P^{(0)}+R-z_0\right)+k\cos(2\alpha)-4(1+k)P_1^{(1)}\sin\alpha\right\}/\left\{4\left[(1+k)P^{(0)}+R-(1+k)z_0\right]\left(P_3^{(2)}-\cos\alpha\right)+4y_0\sin\alpha\right\} \quad , \quad (27)$$

$$F_{21}=-\left\{(1+k)P_1^{(1)}\left(P_3^{(2)}+2P_1^{(2)}R_x\right)+\left(P_3^{(3)}+2P_1^{(3)}R_x\right)\left[(1+k)P^{(0)}+R-(1+k)z_0\right]+(1+k)\left(P_3^{(2)}+2P_1^{(2)}R_x\right)\sin\alpha-\cos\alpha\left[(1+k)P_1^{(1)}+k\sin\alpha\right]\right\}/\left\{2R_x\left[(1+k)P^{(0)}+R-(1+k)z_0\right]\left(P_3^{(2)}-\cos\alpha\right)+2R_xy_0\sin\alpha\right\} \quad , \quad (28)$$

where the expressions for the auxiliary parameters $P_j^{(i)}$ are as follows:

$$P^{(0)}=A_{02}y_0^2+A_{04}y_0^4+A_{06}y_0^6+A_{08}y_0^8+A_{0,10}y_0^{10} \quad , \quad (29)$$

$$P_1^{(1)}=[2A_{02}y_0+4A_{04}y_0^3+6A_{06}y_0^5+8A_{08}y_0^7+10A_{0,10}y_0^9]\cos\alpha \quad , \quad (30)$$

$$P_1^{(2)}=A_{20}+A_{22}y_0^2+A_{24}y_0^4+A_{26}y_0^6+A_{28}y_0^8 \quad , \quad (31)$$

$$P_2^{(2)}=[A_{02}+6A_{04}y_0^2+15A_{06}y_0^4+28A_{08}y_0^6+45A_{0,10}y_0^8]\cos^2\alpha \quad , \quad (32)$$

$$P_3^{(2)}=[2A_{02}y_0+4A_{04}y_0^3+6A_{06}y_0^5+8A_{08}y_0^7+10A_{0,10}y_0^9]\sin\alpha \quad , \quad (33)$$

$$P_1^{(3)}=\left[2A_{22}y_0+4A_{24}y_0^3+6A_{26}y_0^5+8A_{28}y_0^7\right]\cos\alpha \quad , \quad (34)$$

$$P_3^{(3)}=[2A_{02}+12A_{04}y_0^2+30A_{06}y_0^4+56A_{08}y_0^6+90A_{0,10}y_0^8]\cos\alpha\sin\alpha \quad , \quad (35)$$

Due to space limitations, the detailed derivation of the above formulas are provided in Supplement.

The conversion formulas for the local parameters F_{02} and F_{21}, while complex, reveal that they depend solely on $A_{0,2j}$, $A_{2,2j}$. This relationship provides crucial theoretical guidance for freeform surface optimization: only the coefficients $A_{0,2j}$ (for the y^{2j} terms) and $A_{2,2j}$ (for the x^2y^{2j} terms) need to be designated as optimization variables. Higher-order terms involving x, such as x^4y^{2j}, x^6y^{2j}, etc., can be initially neglected. Notably, higher-order coefficients $A_{0,2j}$ and $A_{2,2j}$ (with larger j) are associated with higher powers of y_0, implying their influence on aberrations becomes more pronounced at larger look angles. Therefore, during optimization, freeform coefficients can be introduced progressively. In the initial optimization stage with a small FOR, only low-order terms in y are added as variables. As the FOR is gradually increased during the optimiza-

tion process, higher-order terms in y are successively incorporated. This progressive strategy of adding freeform coefficients is beneficial for enhancing image quality and reducing tolerance sensitivity[29].

4.2 Merit function construction

Conventional optimization methods utilizing spot size as the merit function require tracing a substantial number of real rays. For systems incorporating freeform surfaces with numerous parameters, this approach is computationally slow and prone to convergence to local minima. In contrast, calculating aberration coefficients requires tracing only three rays (OAR, marginal ray, and chief ray), resulting in significantly faster computation. Research indicates that the solution space topography for aberration coefficients closely resembles that of the spot[30]. This suggests that employing an aberration-based merit function can facilitate rapid convergence to the global optimal region of the solution space, after which a spot-size-based merit function can be used for fine optimization, thereby improving overall efficiency. Consequently, we construct the merit function using aberration coefficients as follows:

$$\begin{aligned} MF = & w_1\left\{(W_{02002,\text{total}})^2+(W_{03001,\text{total}})^2\right\}+ \\ & w_2\left\{(W_{02002,\text{dome}})^2+(W_{03001,\text{dome}})^2\right\}+ \\ & w_3\left\{\sum_{i=1}^{4}(W_{02002,\text{surf},i})^2+\sum_{i=1}^{4}(W_{03001,\text{surf},i})^2\right\}, \end{aligned} \tag{36}$$

The merit function consists of three parts. W_{total} is the system's total aberration. W_{dome} is the combined aberration contribution of the dome's outer and inner surfaces, enforcing mutual balance to relieve burden on the corrector. W_{surf} is contribution of each dome and corrector surface, minimizing per-surface aberrations to mitigate higher-order aberrations. Weights $w_1 = 1$, $w_2 = 0.1$, and $w_3 = 0.001$ are chosen for this example but can be tuned per system.

Benefiting from the global optimization capability of the software, a spherical meniscus lens can be used as the initial configuration for the arch corrector. The inner surface of the dome is defined as an aspheric surface, while the arch corrector is modeled as two freeform surfaces. The optimization procedure is performed as follows. In the early stage, an aberration-coefficient–based merit function is employed, and a relatively small FOR is set. Only low-order aspheric coefficients and low-order freeform terms are introduced as optimization variables. During the intermediate stage, the FOR is progressively expanded, and higher-order aspheric coefficients and higher-order freeform terms are gradually added to the optimization variables. In the final stage, the merit function is switched to spot size for fine optimization. The two mirrors and the x^4y^{2j} term coefficients of the arch corrector are included as optimization variables to suppress spherical aberration and higher-order aberrations.

5 Design case comparative validation

To validate the effectiveness of the proposed design methodology, comparative studies were conducted across 14 conformal system design cases, generated by combining seven gimbal point positions with two optimization approaches. The gimbal position L_{GP} was varied from 60 mm to 120 mm at 10 mm intervals to establish the initial configurations. The two optimization methods consist of the progressive optimization approach proposed herein and a conventional optimization method, where the latter employs the technique from reference[18] to calculate the initial arch corrector configuration and utilizes spot size as the merit function. System specifications are detailed in Tab. 2, with layouts of six representative cases illustrated in Fig. 7.

Fig. 8 presents the all-field average RMS spot diameters for 14 design cases. The horizontal axis corresponds to seven gimbal positions, while the vertical axis denotes the RMS spot diameter. The

two curves represent the proposed progressive optimization method and the conventional optimization method, respectively. As shown in Fig. 8, the spot diameter increases with increasing L_{GP} for both methods, indicating that the imaging performance degrades as the gimbal point moves farther away from the dome apex. A comparison of the two curves in Fig. 8 shows that, for each initial structure corresponding to a given L_{GP}, the system obtained using the progressive optimization method consistently exhibits a smaller spot diameter than that achieved with the conventional method, demonstrating the superior performance of the proposed approach. When the initial structure is selected with L_{GP} = 60 mm and optimized using the progressive method, the resulting system achieves the best imaging quality, with a spot diameter of 6.7 μm. In contrast, conventional designs typically adopt an initial structure with L_{GP} = 120 mm combined with conventional optimization[23], yielding a spot diameter of 16 μm. Consequently, the imaging quality of the optical system designed using the proposed method is improved by a factor of about 2.4× compared with that obtained using the conventional approach.

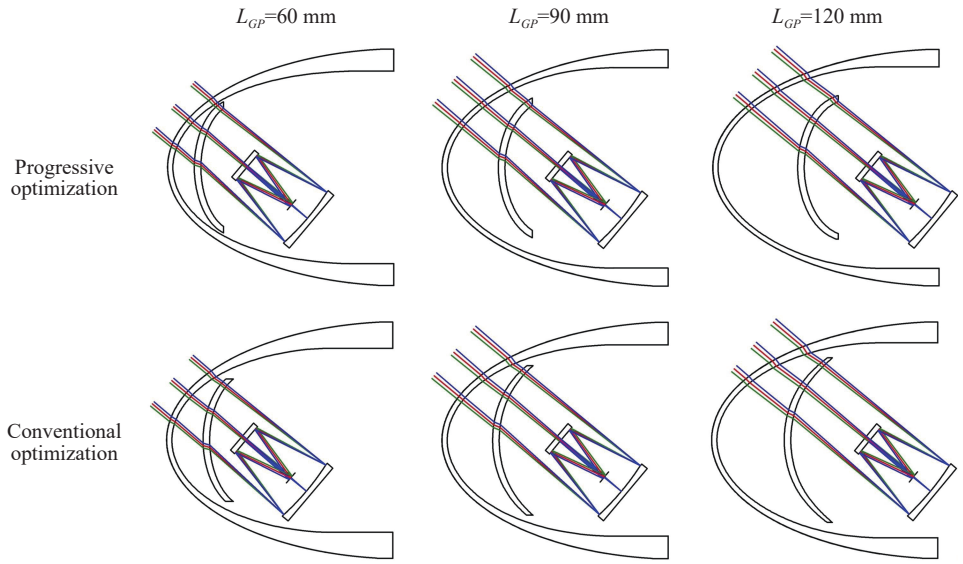

Fig. 7 Conformal system layout obtained by two optimization methods at different gimbal positions.

Tab. 2 Specifications of the system.

Parameter	Specification
Material of dome	ZnS
Fineness ratio (L/D)	1
Diameter of dome (D)	180 mm
Shape of dome	Ellipsoid
Thickness of dome	4 mm
Wavelength	3.7–4.8 μm
Field of regard (FOR)	±40°
Field of view (FOV)	2°×2°
Entrance pupil diameter	45 mm
F-number	2
Pixel size	1.2 μm

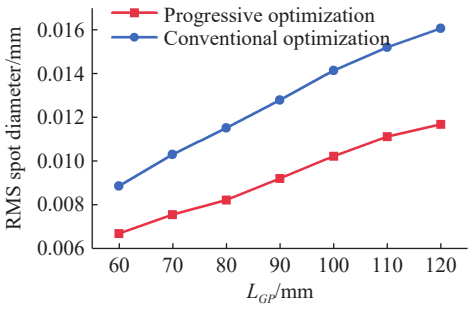

Fig. 8 Average RMS spot diameter of the conformal systems obtained by two optimization methods at different L_{GP}.

Fig. 9 shows the modulation transfer function (MTF) curves at a 40° look angle for six representative cases. The left column plots the MTF of systems obtained by the proposed progressive optimiz-

ation method, while the right column shows the MTF of systems obtained by the conventional optimization method. The three horizontal rows from top to bottom correspond to initial structures with L_{GP} = 60 mm, L_{GP} = 90 mm, and L_{GP} = 120 mm, respectively. A comparison between the left and right columns of Fig. 9 indicates that, for each initial structure, the MTF produced by the progressive optimization is higher than that produced by the conventional method, demonstrating the superior performance of the progressive approach. A comparison of the three rows shows that the MTF decreases markedly for both optimization methods as L_{GP} increases, which indicates that initial structures with the gimbal point closer to the dome apex yield better imaging performance. In particular, when the initial structure with L_{GP} = 60 mm is optimized using the progressive method, the resulting system attains the best imaging performance: the MTF at the Nyquist frequency (42 lp/mm) exceeds 0.4, approaching the diffraction limit and satisfying the performance requirements of conformal optical systems. Together with the results in Fig. 8, Fig. 9 provides strong validation for the effectiveness of selecting initial structures based on aberration theory and for the freeform-surface optimization strategy presented in this work.

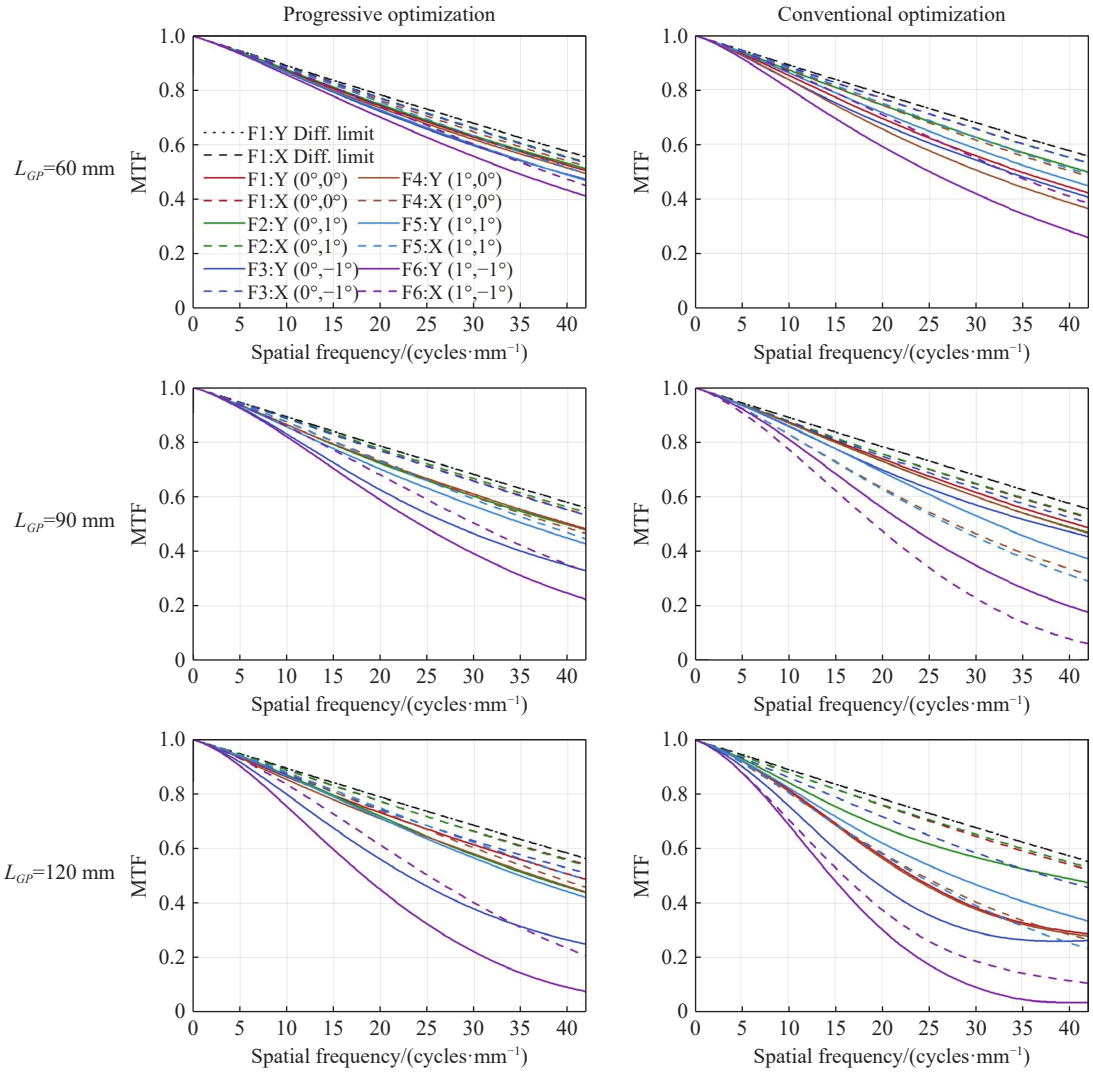

Fig. 9 MTF of the conformal systems obtained by two optimization methods at different L_{GP} when look angle is 40°.

6 Conclusion

This paper extends the plane-symmetric aberration theory to conformal optical systems by establishing a conversion relationship between global and local surface parameters, thereby enabling analytical computation of individual surface aberration contributions. Based on this theoretical foundation, a two-step design methodology is proposed: first, determination of the optimal gimbal position through minimization of the dome outer surface's aberration contribution; second, optimization of the arch corrector via progressive introduction of aberration- related freeform parameters and construction of an aberration-coefficient-based merit function.

Validation through 14 comparative design cases reveals that systems designed using this method achieve an average RMS spot diameter of 6.7 μm across the ±40° field of regard, with modulation transfer function performance approaching the diffraction limit—yielding a 2.4× improvement in imaging quality compared with conventional design methods. This approach provides systematic theoretical guidance for conformal optical system design and substantially reduces the empiricism associated with traditional trial-and-error optimization.

——中文对照版——

1 引 言

现代导弹整流罩为获得更优的空气动力学性能，其外形已由传统的半球形发展为流线型轮廓。共形光学系统是指优先满足非成像性能指标（如空气动力学特性）的光学系统。导弹导引头采用扫描工作模式，整流罩内部的成像系统绕万向节点旋转。对于特定观察视角，整流罩仅部分区域参与成像，且该区域随视角变化而改变，导致整流罩引入的像差具有视角依赖性，此类像差称为动态像差。动态像差的校正是共形光学系统设计面临的核心挑战。

当观察视角非零时，整流罩参与成像的区域不再具有旋转对称性，致使传统赛德尔像差理论难以适用。研究者普遍采用 Zernike 多项式表征共形系统的像差特性，并针对多种整流罩面型开展了像差分析，涵盖圆锥曲面[1-3]、von Kármán 型表面[4-5] 及 Haack 型表面[6] 等。随着像差理论的发展，近年来针对非旋转对称系统涌现出多种像差计算方法，如节点像差理论[7-10]、李代数法[11]、解析法[12-14] 等。这些方法已在离轴三反[15-16]、光谱仪[13]、软 X 射线和真空紫外光学系统[17] 等设计中成功应用。然而，据目前公开文献报道，尚未见将非旋转对称系统像差理论应用于共形系统的研究案例。

为校正共形整流罩引入的动态像差，需在整流罩与成像系统间引入校正元件。经典的像差校正器可分为固定式、运动式和拱形式三类，其中拱形校正器兼具非对称面型的灵活性与无驱动电机的可靠性，优势明显。拱形校正器的初始结构可通过数值求解 Wassermann-Wolf 微分方程获得，再经优化完成最终设计[18]。近年来亦涌现出新的像差校正方案，包括透镜阵列[19-20]、衍射面[21]、整流罩面型优化[22-23] 及波前编码[24-25] 等。但这些方案在加工难度、制造成本或响应速度等方面尚存不足，而拱形校正器的加工与检测技术已较为成熟[26]，因此仍是当前主流选择。

尽管共形光学研究已取得长足进展，但现有设计方法仍缺乏充分的理论指导，过度依赖试错优化与经验判断。当前 Zernike 像差特性分析仅局限于系统总像差的表征，设计者无法基于单一表面的面型参数解析计算其像差贡献。这一理论缺失使得针对特定像差类型高效反演调整面型参数极为困难，导致设计过程呈现较强的经验依赖性。

为克服上述局限，本文拓展了平面对称系统像差理论，提出一种基于像差解析计算的共形光学系统设计方法，为设计过程提供理论支撑。第 2 节推导全局面型参数与局域面型参数的转换关系，将平面对称系统像差理论拓展应用于共形系

统。第 3 节阐述设计方法第一步：通过最小化整流罩外表面的像差贡献，确定最优万向节点位置，为初始结构选取提供理论判据。第 4 节介绍设计方法第二步：逐步引入与像差相关的自由曲面参数作为优化变量，并构建基于像差系数的评价函数，实现拱形校正器的高效优化。第 5 节通过与传统设计方法的对比分析，验证本文所提方法在成像质量提升方面的显著优势。

2　平面对称系统像差理论的拓展

2.1　现有像差理论

Sasián[27] 建立了平面对称系统的像差表达式：

$$W(\boldsymbol{H},\boldsymbol{\rho})=\sum_{k,m,n,p,q}^{\infty}W_{i,j,n,p,q}(\boldsymbol{H}\cdot\boldsymbol{H})^{k}(\boldsymbol{\rho}\cdot\boldsymbol{\rho})^{m}(\boldsymbol{H}\cdot\boldsymbol{\rho})^{n}(\boldsymbol{i}\cdot\boldsymbol{H})^{p}(\boldsymbol{i}\cdot\boldsymbol{\rho})^{q}\quad,\tag{1}$$

其中下标i,j,k,m,n,p,q为整数，满足$i=2k+n+p$，$j=2m+n+q$。$W_{i,j,n,p,q}$为像差系数，$\boldsymbol{H}$为归一化视场矢量，$\boldsymbol{\rho}$为归一化光瞳矢量，$\boldsymbol{i}$为指向 Y 轴正方向的单位矢量。相较于旋转对称系统，平面对称系统的像差表达式增加了$(\boldsymbol{i}\cdot\boldsymbol{H})^{p}$和$(\boldsymbol{i}\cdot\boldsymbol{\rho})^{q}$两项，从而衍生出更多像差类型。

像差项根据矢量点积的数量$k+m+n+p+q$进行分组。表 1 列出了前三组像差项，其中“常量”“线性”“二次”等前缀表征像差的视场依赖性，即视场矢量的指数。当$p,q=0$时，$W_{i,j,n,0,0}$对应旋转对称系统的像差系数，即第三组中底部所列的像差项。

Liu[13] 基于局域面型参数与光线追迹数据，建立了平面对称系统的像差解析计算方法。局域面型定义为球面基底叠加关于 YZ 平面对称的自由曲面，其四阶近似表达式为：

$$z'\approx\frac{r'^{2}}{2R_x}+\frac{r'^{4}}{8R_x^{3}}+F_{02}y'^{2}+F_{21}x'^{2}y'+F_{03}y'^{3}+F_{40}x'^{4}+F_{22}x'^{2}y'^{2}+F_{04}y'^{4}\quad,\tag{2}$$

其中$r'^{2}=x'^{2}+y'^{2}$，x'，y'为局域坐标，z'为局域矢高。R_x为弧矢曲率半径，F_{02}，F_{21}，F_{03}，F_{40}，F_{22}，F_{04}为自由曲面系数，统称为局域面型参数。鉴于高阶面型参数对第三组像差无贡献[13]，局域面型仅保留到四阶项即可。

像差计算基于三条特征光线的追迹数据：对光轴光线（Optical axis ray, OAR）进行真实光线追迹，获取入射角I与折射角I'；对弧矢方向的边缘光线与主光线进行近轴光线追迹，获得光线高度x_a，x_b及光线角度u_{ax}，u'_{ax}，u_{bx}，u'_{bx}。弧矢方向近轴光线追迹公式为：

$$x_{i+1}=x_i+u'_{xi}t_i\quad,\tag{3}$$

$$n'_iu'_{xi}=n_iu_{xi}-x_i\phi_{xi}\quad,\tag{4}$$

$$u_{xi+1}=u'_{xi}\quad,\tag{5}$$

其中ϕ_{xi}为表面在弧矢方向的光焦度，有

$$\phi_{xi}=\frac{n'_i\cos I'_i-n_i\cos I_i}{R_{xi}}\quad,\tag{6}$$

像差由固有像差和诱导像差共同构成，其中固有像差计算公式可直接反映局域面型参数与像差系数的关系。以W_{02002}和W_{03001}为例：

$$W_{02002}=-\frac{1}{2}\Delta\left(\frac{u_{ax}C}{n}\right)\frac{x_a}{\cos^{2}I'}+\Delta(n\cos I)F_{02}\frac{x_a^{2}}{\cos^{2}I'}\quad,\tag{7}$$

$$W_{03001}=-\frac{A}{2}\Delta\left(\frac{u_{ax}C}{n}\right)\frac{x_a}{\cos I'}-\frac{1}{2R_x}\Delta\left(\frac{u_{ax}C^{2}}{n}\right)\frac{x_a^{2}\tan I'}{\cos I'}+\Delta(n\cos I)\left(F_{21}+F_{02}\frac{\tan I'}{R_x}\right)\frac{x_a^{3}}{\cos I'}\quad,\tag{8}$$

式中$\Delta(\cdot)$表示折射前后物理量的改变，A，C为折射不变量，有

$$A=n\left(u_{ax}+\frac{x_a\cos I}{R_x}\right)\quad,\tag{9}$$

$$C=n\sin I\quad,\tag{10}$$

由上式可见，W_{02002}主要与局域面型参数F_{02}相关，而W_{03001}主要与F_{21}相关。这一解析关系为共形系统的像差分析与面型优化奠定了理论基础。

2.2　拓展至共形系统

在现有像差理论中，面型在局域坐标系下描述，其原点位于光轴光线（OAR）与表面的交点，Z 轴沿该点法线方向（见图 1 红色坐标系 X’Y’Z’）。然而在光学设计软件中，面型在全局坐标系下定义，其原点位于表面顶点，Z 轴沿顶点法线方向（见图 1 蓝色坐标系 XYZ）。对于共形系统，当视角（Look angle, LA）非零时，光轴光线与表面交

点偏离顶点，导致两坐标系不重合。此时无法直接应用像差理论，需先将全局面型参数转换为局域面型参数，进而计算像差系数。

共形系统常用的全局面型包括圆锥曲面、非球面及 XY 多项式自由曲面。本小节推导圆锥曲面的面型参数转换公式作为示例，非球面和 XY 多项式的推导过程见补充文档。

圆锥曲面的全局面型表达式为：

$$z=\frac{cr^2}{1+\sqrt{1-(1+k)c^2r^2}}\quad , \tag{11}$$

其中 $r^2=x^2+y^2$，x，y 为全局坐标，z 为全局矢高。c 为顶点曲率，k 为圆锥系数。局域面型表达式为式 (2)，转换目标即根据全局面型参数 c，k 及交点坐标 $(0,y_0,z_0)$ 求解局域面型参数 R_x，F_{02}，F_{21}，F_{03}，F_{40}，F_{22}，F_{04}。

设全局面型满足的曲面方程为 $F(x,y,z)=0$，对于圆锥曲面有

$$F(x,y,z)=z^2(1+k)c-2z+c\left(x^2+y^2\right)=0\quad , \tag{12}$$

如图 1 (b) 所示，将全局坐标系平移至交点 $(0,y_0,z_0)$ 后旋转 α 角，即可得到局域坐标系。全局坐标 x,y,z 与局域坐标 x',y',z' 的变换关系为：

$$\begin{cases} x=x' \\ y=\cos\alpha y'+\sin\alpha z'+y_0 \\ z=-\sin\alpha y'+\cos\alpha z'+z_0 \end{cases} \tag{13}$$

将式 (13) 代入式 (12)，得到局域坐标系下的曲面方程 $G(x',y',z')=0$，有

$$\begin{aligned} G(x',y',z')=&(-\sin\alpha y'+\cos\alpha z'+z_0)^2(1+k)c-\\ &2(-\sin\alpha y'+\cos\alpha z'+z_0)+\\ &c\left[x'^2+(\cos\alpha y'+\sin\alpha z'+y_0)^2\right]=\\ &0\quad , \end{aligned} \tag{14}$$

其中 $z_0,\sin\alpha,\cos\alpha$ 均可表示为 y_0 的函数：

$$z_0=\frac{1-\sqrt{1-(1+k)c^2y_0^2}}{(1+k)c}\quad , \tag{15}$$

$$\sin\alpha=\frac{-cy_0}{\sqrt{1-kc^2y_0^2}}\quad , \tag{16}$$

$$\cos\alpha=\frac{\sqrt{1-(1+k)c^2y_0^2}}{\sqrt{1-kc^2y_0^2}}\quad , \tag{17}$$

将式 (15)–(17) 代入式 (14)，化简得到

$$\begin{aligned} G(x',y',z')=&cx'^2+\frac{cy'^2}{1-c^2ky_0^2}-2z'\sqrt{1-c^2ky_0^2}+\\ &y'z'\frac{2c^2ky_0\sqrt{1-c^2(1+k)y_0^2}}{1-c^2ky_0^2}-\\ &z'^2\frac{c\left[-1+c^2k^2y_0^2+k\left(-1+2c^2y_0^2\right)\right]}{1-c^2ky_0^2}=\\ &0\quad , \end{aligned} \tag{18}$$

将局域面型表达式 (2) 代入上式，得到关于 x',y' 的多项式 $G(x',y')=0$，它包含 x'^2，y'^2，x'^2y'，y'^3，x'^4，$x'^2y'^2$，y'^4 项。令各项系数为零，即可解得局域面型参数的表达式为：

$$R_x=\frac{\sqrt{1-c^2ky_0^2}}{c}\quad , \tag{19}$$

$$F_{02}=\frac{c^3ky_0^2}{2\left(1-c^2ky_0^2\right)^{3/2}}\quad , \tag{20}$$

$$F_{21}=\frac{c^3ky_0\sqrt{1-c^2(1+k)y_0^2}}{2\left(1-c^2ky_0^2\right)^2}\quad , \tag{21}$$

$$F_{03}=\frac{c^3ky_0\sqrt{1-c^2(1+k)y_0^2}}{2\left(1-c^2ky_0^2\right)^3}\quad , \tag{22}$$

$$F_{40}=\frac{c^3k-c^5k(1+k)y_0^2}{8\left(1-c^2ky_0^2\right)^{5/2}}\quad , \tag{23}$$

$$F_{22}=\frac{c^3k\left[1+c^2ky_0^2-c^4k(3+2k)y_0^4\right]}{4\left(1-c^2ky_0^2\right)^{7/2}}\quad , \tag{24}$$

$$\begin{aligned} F_{04}=&c^3k\left[1+(1+3k)c^2y_0^2-k(7+4k)c^4y_0^4+\right.\\ &\left.k^2c^6y_0^6\right]/\left[8\left(1-c^2ky_0^2\right)^{9/2}\right]\quad , \end{aligned} \tag{25}$$

至此，局域面型参数 R_x，F_{02}，F_{21}，F_{03}，F_{40}，F_{22}，F_{04} 已完全由全局面型参数 c，k 及交点坐标 y_0 表示，面型参数转换关系推导完成。结合光线追迹数据，即可进一步计算各表面的像差贡献。

3 万向节点位置的选取

图 2 为共形光学系统示意图，成像系统被安

置在万向支架上，其摆动角度称作视角（Look angle, LA），最大视角称作观察视场（Field of regard, FOR）。万向节点位置是影响初始结构的关键参数。

现有文献虽已探讨了系统总像差随万向节点位置的变化规律，并指出其对总像差影响微弱[3]，但该结论尚不完善。整流罩由内外两个表面构成，系统总像差实为内外表面像差相互平衡后的残余量，与整流罩几何特性的关联较弱。为深入揭示万向节点位置与像差的内在关系，本文从外表面像差贡献的角度开展了系统性分析。

以椭球形整流罩为例，其长度为 180 mm，长径比为 1，全局面型参数为顶点曲率半径 R = 45 mm，圆锥系数 k = −0.75，材料选用 ZnS。成像系统采用接近理想成像的两反射镜系统，光阑置于主镜，万向节点位于次镜顶点。图 3 展示了万向节点距整流罩顶点分别为 60 mm 与 120 mm 的系统布局。在同一观察视场范围内，万向节点越靠近整流罩顶点，整流罩参与成像的区域越集中于顶端。

鉴于共形系统的主要像差为常量像散与常量彗差[1-3]，本文聚焦对应的像差系数 W_{02002} 与 W_{03001}。对这两项像差影响最显著的局域面型参数分别为 F_{02} 与 F_{21}，由式 (20) 和式 (21) 可知，它们均为 OAR 交点坐标 y_0 的函数，其变化曲线如图 4 所示，其中 L_{GP} 表征万向节点与整流罩顶点的间距。图 4 表明，当观察视场为±40°且 L_{GP} 在 60–120 mm 范围时，随着 L_{GP} 增大，F_{02} 的动态范围显著增大，而 F_{21} 因存在极值点导致动态范围不变。

这一几何特性致使 W_{02002} 的动态范围随 L_{GP} 增大而急剧增大，而 W_{03001} 的动态范围则几乎保持不变，如图 5 和图 6 所示。综合而言，万向节点越靠近整流罩顶点，整流罩外表面的像差贡献越小。

较大的像差面贡献往往伴随显著的高阶像差，导致系统总像差难以平衡校正[28]。基于像差面贡献应尽量小的设计原则，本文提出初始结构选取准则：万向节点应尽量靠近整流罩顶点。对于上述椭球形整流罩，确定 L_{GP} = 60 mm 为最优万向节点位置。

4　拱形校正器的优化

4.1　优化变量逐步设置

拱形校正器采用双平面对称的自由曲面，其全局面型表达式为：

$$z=\frac{cr^2}{1+\sqrt{1-(1+k)c^2r^2}}+\sum_{i,j=0}^{5}A_{2i,2j}x^{2i}y^{2j}\quad,\quad(26)$$

其中 $r^2=x^2+y^2$，x, y 为全局坐标，z 为矢高，c 为顶点曲率，k 为圆锥系数，$A_{2i,2j}$ 为 $x^{2i}y^{2j}$ 项的自由曲面系数。鉴于系统关于 YZ 与 XZ 平面双对称，表达式仅含 y' 与 z' 的偶次幂。

为应用像差理论，需将全局面型参数转换为局域面型参数。其中 F_{02} 与 F_{21} 的转换公式为：

$$F_{02}=\left\{-2P_1^{(1)2}-k\left[1+2P_1^{(1)2}-4\left(P_1^{(2)}-P_2^{(2)}\right)\left(P^{(0)}-z_0\right)\right]+4\left(P_1^{(2)}-P_2^{(2)}\right)\left(P^{(0)}+R-z_0\right)+k\cos(2\alpha)-4(1+k)P_1^{(1)}\sin\alpha\right\}/\left\{4\left[(1+k)P^{(0)}+R-(1+k)z_0\right]\left(P_3^{(2)}-\cos\alpha\right)+4y_0\sin\alpha\right\}\quad,\quad(27)$$

$$F_{21}=-\left\{(1+k)P_1^{(1)}\left(P_3^{(2)}+2P_1^{(2)}R_x\right)+\left(P_3^{(3)}+2P_1^{(3)}R_x\right)\left[(1+k)P^{(0)}+R-(1+k)z_0\right]+(1+k)\left(P_3^{(2)}+2P_1^{(2)}R_x\right)\sin\alpha-\cos\alpha\left[(1+k)P_1^{(1)}+k\sin\alpha\right]\right\}/\left\{2R_x\left[(1+k)P^{(0)}+R-(1+k)z_0\right]\left(P_3^{(2)}-\cos\alpha\right)+2R_xy_0\sin\alpha\right\}\quad,\quad(28)$$

其中辅助参量 F_{40} 的表达式为：

$$P^{(0)}=A_{02}y_0^2+A_{04}y_0^4+A_{06}y_0^6+A_{08}y_0^8+A_{0,10}y_0^{10}\quad(29)$$

$$P_1^{(1)}=[2A_{02}y_0+4A_{04}y_0^3+6A_{06}y_0^5+8A_{08}y_0^7+10A_{0,10}y_0^9]\cos\alpha\quad,\quad(30)$$

$$P_1^{(2)}=A_{20}+A_{22}y_0^2+A_{24}y_0^4+A_{26}y_0^6+A_{28}y_0^8\quad,\quad(31)$$

$$P_2^{(2)}=[A_{02}+6A_{04}y_0^2+15A_{06}y_0^4+28A_{08}y_0^6+45A_{0,10}y_0^8]\cos^2\alpha\quad,\quad(32)$$

$$P_3^{(2)}=[2A_{02}y_0+4A_{04}y_0^3+6A_{06}y_0^5+8A_{08}y_0^7+10A_{0,10}y_0^9]\sin\alpha\quad,\quad(33)$$

$$P_1^{(3)}=\left[2A_{22}y_0+4A_{24}y_0^3+6A_{26}y_0^5+8A_{28}y_0^7\right]\cos\alpha\quad,\quad(34)$$

$$P_3^{(3)}=[2A_{02}+12A_{04}y_0^2+30A_{06}y_0^4+56A_{08}y_0^6+90A_{0,10}y_0^8]\cos\alpha\sin\alpha\quad,\quad(35)$$

由于篇幅所限，上述公式的详细推导见补充文档。

尽管F_{02}与F_{21}表达式较为复杂，仍可明晰其关联的全局面型参数。由辅助参量的表达式可知，F_{02}与F_{21}仅取决于x的零阶系数$A_{0,2j}$与二阶系数$A_{2,2j}$，这为自由曲面优化提供了明确的理论指导：仅需将y^{2j}项系数$A_{0,2j}$与x^2y^{2j}项系数$A_{2,2j}$设为优化变量，而关于x的高次项（如x^4y^{2j}，x^6y^{2j}等）可不予考虑。值得注意的是，当阶次j较大时，关于y的高阶系数$A_{0,2j}$与$A_{2,2j}$伴随着y_0的高阶项，表明其影响随视角增大而增强。因此，优化过程可采用渐进式变量添加策略：初期设定较小观察视场，仅引入y的低阶项作为优化变量；待视场逐步扩大后，再递增添加高阶系数。此渐进式方法有助于提升成像质量并降低公差敏感度[29]。

4.2 评价函数构建

传统优化方法通常以像面光斑尺寸作为评价函数，需追迹大量真实光线。对于含自由曲面的系统，参数众多导致优化效率低且易陷入局部极值。相比之下，像差系数仅需追迹光轴光线、边缘光线与主光线三条特征光线即可快速计算。研究表明，像差系数解空间与模糊光斑解空间在地形特征上高度相似[30]，故可先采用像差评价函数引导优化快速收敛至全局最优解空间，再切换至光斑评价函数进行精细优化，从而显著提升优化效率。基于上述思想，本文构建如下评价函数：

$$\begin{aligned} MF =& w_1\left\{\left(W_{02002,\mathrm{total}}\right)^2+\left(W_{03001,\mathrm{total}}\right)^2\right\}+ \\ & w_2\left\{\left(W_{02002,\mathrm{dome}}\right)^2+\left(W_{03001,\mathrm{dome}}\right)^2\right\}+ \\ & w_3\left\{\sum_{i=1}^{4}\left(W_{02002,\mathrm{surf},i}\right)^2+\sum_{i=1}^{4}\left(W_{03001,\mathrm{surf},i}\right)^2\right\}, \end{aligned} \tag{36}$$

式中，下标“total”表征系统总像差，用于控制整体像差水平；下标“dome”表征整流罩的像差贡献，用于约束内外表面像差平衡，以减轻校正器负担；下标“surf”表征各表面像差贡献（考虑整流罩内外表面及校正器两表面共四个面），用于抑制高阶像差，便于后续精细优化。权重系数w_1，w_2，w_3可根据系统特性灵活调整，本示例中取$w_1=1$，$w_2=0.1$，$w_3=0.001$。

得益于全局优化算法，拱形校正器可从球面弯月透镜起步。将整流罩内表面设为非球面，拱形校正器设为自由曲面，优化流程如下：初期采用基于像差系数的评价函数，设定较小观察视场，仅引入低阶非球面与自由曲面系数作为优化变量；中期逐步扩大视场并递增高阶系数；后期切换至光斑尺寸评价函数进行精细优化，同时增加拱形校正器的k项系数与两反射镜面型作为优化变量，以抑制球差与高阶残余像差。

5 设计案例对比验证

为验证本文所提设计方法的有效性，对 14 组共形系统设计案例开展对比研究，由 7 个万向节点位置与 2 种优化方法组合而成。万向节点间距L_{GP}在 60–120 mm 范围内以 10 mm 为间隔选取 7 个位置作为初始结构。优化方法包括本文所提逐步优化法与传统优化法，其中传统优化法采用文献[18]方法计算拱形校正器初始结构，并以光斑尺寸作为评价函数。系统指标如表 2 所示，图 7 给出其中 6 个典型案例的布局。

图 8 展示了 14 个设计案例的所有视场平均 RMS 点列图半径。横轴对应 7 个万向节点位置，纵轴对应 RMS 点列图直径，两条曲线分别对应本文所提逐步优化法与传统优化法。如图 8 所示，随着L_{GP}增大，两种优化方法均表现出点列图直径增大，这表明随着万向节点远离整流罩顶点，系统的成像质量退化。对比图 8 中两条曲线，对于每个L_{GP}对应的初始结构，逐步优化法所得系统的点列图半径均小于传统优化法，这表明逐步优化法的效果优于传统优化法。当初始结构选取$L_{GP}=60$ mm并采用逐步优化法时，所获系统成像质量达到最佳，其点列图直径为 6.7 μm。而传统设计多采用$L_{GP}=120$ mm附近的初始结构[23]并结合传统优化方法，所得系统点列图直径达 16 μm。因此采用本文所提设计方法得到光学系统的成像质量为传统方法的 2.4 倍。

图 9 呈现了 6 个典型案例在 40°视角时的调制传递函数（MTF）曲线。左纵栏为采用逐步优化法得到系统的 MTF，右纵栏为采用传统优化法得到系统的 MTF。从上至下的三横行分别对应着L_{GP}取 60 mm、90 mm、120 mm 的三种初始结构。对比图 9 左右两栏，对于每个初始结构，逐步优化法所得系统的 MTF 均高于传统优化法，这表明逐步优化法的效果更佳。对比图 9 上下三行，随着L_{GP}增大，两种优化方法所得系统的 MTF 均

下降明显，这表明万向节点靠近整流罩顶点的初始结构更佳。当初始结构选取α并采用逐步优化法时，所获系统成像质量最佳，MTF 在奈奎斯特频率（42 lp/mm）高于 0.4，成像质量接近衍射极限，能够满足共形光学系统的使用需求。图 8 与图 9 的结果充分验证了基于像差理论的初始结构选取与自由曲面优化策略的有效性。

6　结　论

本文将平面对称像差理论拓展至共形系统，建立了全局面型与局域面型的参数转换关系，实现了各表面像差贡献的解析计算。基于该理论提出两步式设计方法：通过最小化整流罩外表面像差贡献确定最优万向节点位置，并采用逐步引入像差相关自由曲面参数与构建像差系数评价函数的策略，完成拱形校正器优化。

对比 14 组设计案例表明：采用本文方法所得系统在±40°观察视场内平均 RMS 点列图直径降至 6.7 μm，调制传递函数接近衍射极限，成像质量达到传统设计方法的 2.4 倍。该方法为共形光学系统设计提供了理论指导，显著减少了设计盲目性。

References:

[1] LIU Y M, MA J, MA H P, *et al*.. Zernike aberration characteristics of precision conformal optical windows[J]. *Proceedings of SPIE*, 2010, 7544: 75443W.

[2] SHI Y T, ZHANG W, CHEN SH Q, *et al*.. Research of aberration characteristics of conicoidal conformal optical domes[J]. *Optik*, 2015, 126(23): 3582-3588.

[3] DANG F Y, ZHANG W, CHEN SH Q, *et al*.. Basic geometry and aberration characteristics of conicoidal conformal domes[J]. *Applied Optics*, 2016, 55(31): 8713-8721.

[4] JU L, LIU Y L, MING Y, *et al*.. Aberration characteristic correlation configuration optimization of a conformal dome based on the von Karman surface[J]. *Optics Express*, 2021, 29(17): 27350-27361.

[5] JU L, ZHANG Y Q, MING Y, *et al*.. Geometric characteristics and aberration characteristics of conformal dome based on von Karman surface[J]. *Optics Communications*, 2022, 507: 127472.

[6] FAN W W, ZHANG W ZH, FAN ZH G. Research on aberration correction methods of conformal dome based on haack curve[J]. *Optics Communications*, 2024, 565: 130676.

[7] YEŞILTEPE M, BAUER A, KARCI Ö, *et al*.. Sigma vector calculations in nodal aberration theory and experimental validation using a Cassegrain telescope[J]. *Optics Express*, 2023, 31(25): 42373-42387.

[8] WAN K, GU ZH Y, YAN CH X. An analytic expression for the field dependence of three-order Zernike aberrations in decentered and/or tilted optical systems[J]. *Optics Communications*, 2024, 565: 130696.

[9] ZHANG SH, ZHAO X, LI D. Iterative paraxial tracing-based model for solving the aberration field decenter vector in aberration analysis[J]. *Optics Express*, 2025, 33(17): 37046-37060.

[10] JIANG Y SH, WANG L J, ZENG X F, *et al*.. Aberration field distribution characterization and tolerance analysis based on nodal aberration theory[J]. *Optics Express*, 2025, 33(23): 49313-49328.

[11] BARION A, ANTHONISSEN M J H, TEN THIJE BOONKKAMP J H M, *et al*.. Computing aberration coefficients for plane-symmetric reflective systems: a Lie algebraic approach[J]. *Journal of the Optical Society of America A*, 2023, 40(6): 1215-1224.

[12] LIU Y X, STEIDLE J, ROLLAND J P. Intrinsic aberration coefficients for plane-symmetric optical systems consisting of spherical surfaces[J]. *Journal of the Optical Society of America A*, 2023, 40(2): 378-387.

[13] LIU Y X. *Analytical aberration theory for plane-symmetric optical systems and its application in the analysis of distortion in freeform spectrometers*[D]. New York: University of Rochester, 2024.

[14] LIU Y X, ROLLAND J P. Analytical aberration theory for plane-symmetric optical systems and its application in distortion analysis of spectrometers[J]. *Journal of the Optical Society of America A*, 2025, 42(3): 362-377.

[15] ZHANG SH, ZHAO X, LI D, *et al*.. High-precision analysis of aberration contribution of Zernike freeform surface terms for non-zero field of view[J]. *Optics Express*, 2024, 32(3): 3167-3183.

[16] ZHANG J P, SHI G W, HUANG Y Q, *et al*.. Optimization of optical system for reducing tolerance sensitivity based on the high-order nodal aberration theory[J]. *Optics Express*, 2024, 32(8): 14334-14355.

[17] CAO Y Q. Design method of soft X-ray and vacuum ultraviolet optical system based on plane-symmetric aberration

theory[J]. *Optical Review*, 2022, 29(3): 207-214.

[18] FAN W W, ZHANG W ZH, FAN ZH G. Research on the design method of arch corrector based on Haack conformal dome[J]. *Physics Letters A*, 2025, 531: 130173.

[19] 句源, 赵春竹, 朴明旭, 等. 基于自由曲面透镜阵列的共形整流罩动态像差校正[J]. 光学学报, 2021, 41(9): 0922002.
JU Y, ZHAO C ZH, PIAO M X, *et al*.. Dynamic aberration correction for conformal dome based on free-form lens array[J]. *Acta Optica Sinica*, 2021, 41(9): 0922002. (in Chinese).

[20] 朴明旭, 张博, 王喆, 等. 大扫描视场飞行器共形光学系统设计[J]. 飞控与探测, 2023, 6(2): 10-17.
PIAO M X, ZHANG B, WANG ZH, *et al*.. Design of conformal optical system for aircrafts with large scanning field of view[J]. *Flight Control & Detection*, 2023, 6(2): 10-17. (in Chinese).

[21] ZHANG Y Q, CHANG J, DANG F Y, *et al*.. Dynamic aberrations correction of Roll-Nod conformal seeker based on the diffraction surface and anamorphic asphere surface[J]. *Chinese Optics Letters*, 2020, 18(7): 072201.

[22] JU L, LIU B, FAN ZH G, *et al*.. Adaptive optimization technology of a conformal infrared dome based on the Von Karman surface under hypersonic conditions[J]. *Optics Express*, 2023, 31(14): 22323-22342.

[23] ZHAO C H, CHEN X T, NIU B Q. Design a conformal optical system based on Fermat's principle[J]. *Optics Express*, 2025, 33(10): 21274-21287.

[24] YU J Q, CHEN SH Q, DANG F Y, *et al*.. The dynamic aberrations suppression of conformal optical system by wavefront coding[J]. *Optics Communications*, 2020, 463: 125121.

[25] YU J Q, CHEN SH Q, DANG F Y, *et al*.. The suppression of aero-optical aberration of conformal dome by wavefront coding[J]. *Optics Communications*, 2021, 490: 126876.

[26] ZHAO J B, WANG SH, ZHANG CH Y, *et al*.. Research status and challenges in the manufacturing of IR conformal optics[J]. *Defence Technology*, 2024, 40: 154-172.

[27] SASIÁN J M. How to approach the design of a bilateral symmetric optical system[J]. *Optical Engineering*, 1994, 33(6): 2045-2061.

[28] KIDGER M J. *Intermediate Optical Design*[M]. Bellingham: SPIE Press, 2004: 45.

[29] BAUER A, SCHIESSER E M, ROLLAND J P. Starting geometry creation and design method for freeform optics[J]. *Nature Communications*, 2018, 9(1): 1756.

[30] STURLESI D, O'SHEA D C. Global view of optical design space[J]. *Optical Engineering*, 1991, 30(2): 207-218.

Author Biographies:

YAN Shu-run (2001—), male, from Ezhou, Hubei Province, is a master's degree student. He obtained his bachelor's degree from Wuhan University in 2023 and mainly engages in the research of conformal optics. E-mail: shurunyan@163.com

严舒润(2001—), 男, 湖北鄂州人, 硕士在读, 主要从事共形光学的研究。E-mail: shurunyan@163.com

MENG Qing-yu (1986—), male, from Changchun, Jilin Province, is a Ph.D., researcher, and doctoral supervisor. He mainly engages in the research of optical system design. E-mail: mengqy@ciomp.ac.cn

孟庆宇(1986—), 男, 吉林长春人, 研究员, 博士生导师, 主要从事光学系统设计的研究。E-mail: mengqy@ciomp.ac.cn